ICAS 2021 SHANGHAI
International Council of the Aeronautical Sciences
32nd Congress of the International Council of the Aeronautical Sciences
September 6-10, 2021
Pudong Shangri-La, Shanghai, China

UNSTEADY FLOW SIMULATION AROUND MAIN LANDING GEAR USING HIERARCHICAL CARTESIAN GRID METHOD WITH IMMERSED BOUNDARY METHOD

Taro Imamura[1] & Yoshiharu Tamaki[2]

[1]The University of Tokyo, Tokyo, 113-8656, Japan mailto:imamura@g.ecc.u-tokyo.ac.jp
[2]Tohoku University, Sendai, Miyagi, 980-8579, Japan

Abstract

Among the airframe noise from an aircraft, landing gear noise is one of the dominant noise sources during the approach phase. A hierarchical Cartesian-grid-based flow solver for unsteady flow simulation is used to investigate the noise generated from a realistic landing gear configuration. Flow simulations around multiple configurations by putting on/off the landing gear components are performed. The overall flow field around the complex geometry is investigated in detail based on the time-averaged flow field. Also, the far-field noise is estimated based on Curle's equation assuming that acoustic sources are compact. Relation between the landing gear components and the power spectral density distribution is investigated to understand the dominant noise source of the landing gear.

Keywords: Airframe noise, Landing gear, Computational Aeroacoustics

1. Introduction

Aircraft noise is a critical issue from the viewpoint of environmental protection around the airport. The forecast of air traffic over multiple years is believed to increase even under the current state of the coronavirus outbreak. Thus, reducing the noise during take-off and landing is one of the critical technologies for the sustainable development of the aircraft industry. The aircraft noise consists of two major components, i.e. engine noise and airframe noise. The engine noise is known to be the dominant noise source, especially during the take-off at maximum engine thrust. Meanwhile, airframe noise becomes recognizable during the approach phase at reduced engine thrust. Consideration of all the noise sources is necessary to develop an environment-friendly low-noise aircraft.

Among the airframe noise, landing gear noise is one of the dominant noise sources of an aircraft during the approach phase, just before landing. Landing gear consists of multiple components such as cylinder, piston, doors, side-brace, wheel well, etc. Research on the various landing gear geometries [1-22] is performed both experimentally and numerically to understand the noise source mechanism as well as to reduce the noise. Most of the numerical research uses a body-fitted grid. A structured grid is used for relatively simple landing gear geometry (still very complex for this type of grid) [1,4]. Unstructured grid using tetrahedral mesh and prism layer near the wall [4,8], Cartesian grid with boundary layer grid [9,19,20], seems to be promising methods to calculate the flow around more realistic and complex landing gear geometries. However, the generation of a body-fitted grid around a realistic landing gear is often a painful process. The process will become even worse when flow analysis needs to be performed for multiple configurations. On the other hand, flow solvers based on the non-body-fitted Cartesian grid are gaining more attention. For example, the lattice Boltzmann method (LBM) coupled with a wall function to reproduce the turbulent boundary layer around the wall is used extensively in past research [3,7,10,11,13-16]. The flow solver based on the Navier-Stokes equations can be also developed on a non-body-fitted Cartesian grid [6,22]. We have shown in our previous study [22] by solving a flow around a realistic landing gear. The flow solver based on the non-body-fitted Cartesian grid is advantageous not only because it is easy to generate a grid, but also because it is possible to select a large time step in unsteady flow simulation. This is one of the important parameters defining the overall computational time of the unsteady flow simulation.

The objective of this study is to investigate the noise that is generated from a realistic landing gear configuration. Flow simulations around multiple configurations by putting on/off the landing gear components are performed by using the Navier-Stokes equation-based flow solver on the non-body-fitted Cartesian grid. A flow solver is called UTCart (the University of Tokyo Cartesian-grid-based automatic flow solver) that is an in-house code developed by the Aircraft Design Laboratory of the University of Tokyo [23-27]. Near wall boundary condition is imposed using an immersed boundary method, and DDES based turbulence model modified for the applications on the non-body-fitted Cartesian grid is used to simulate the unsteady flow.

The structure of this paper is as follows. In section 2, an overview of the flow solver (UTCart) is described. In section 3, the landing gear geometry and the flow conditions for the simulations are explained. Section 4 presents the results and discussion. Finally, section 5 concludes this paper.

2. Numerical Methods

2.1 The Baseline Grid Generator and Flow Solver (UTCart)

The specification of the baseline flow solver UTCart is described. UTCart consists of two parts: the grid generation and the flow solver.

First, the hierarchical Cartesian grid is generated automatically using tree data structures, i.e., the quad-tree (2D) or oct-tree (3D). The shapes of input objects are defined by sets of line segments in 2D or Standard Triangulated Language files (i.e., sets of triangular facet segments) in 3D. Then, binary-tree structures and bounding boxes are constructed for each object to search the nearest line/facet. The cells intersecting the input object are treated as wall cells. In addition, the cells inside and outside the input object are classified as body and fluid cells, respectively. We control the grid distribution around the input object by the following two options. The first option is the number of cells in each layer of the same cell size. Figure 1 illustrates the case where the minimum number of cells in each layer is set to four. In this case, the minimum cell size near the wall (the first layer) is doubled after at least four cells of the same size, and this rule continues to the far-field boundary. The number of cells in each layer is controlled as necessary. The second option is the refinement box used to refine a specific area of the computational domain uniformly. The minimum/maximum coordinates of the rectangular and the uniform cell size inside the box specify the refinement box. After the hierarchical Cartesian grid generation, the grid is partitioned using the METIS library [28] for a parallel computation based on the message passing interface. In each divided grid domain, sleeve cells are specified for the communication between the domains [23].

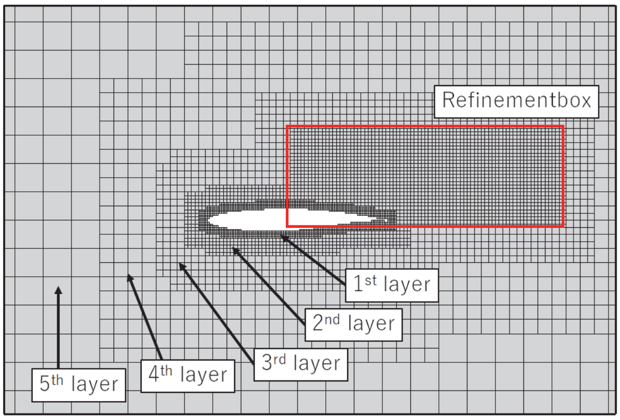

Figure 1 – The layers and the refinement box of the generated grid.

In the second step, a flow calculation is performed. The flow simulation by UTCart is based on the compressible Euler/Navier–Stokes equations in a conservation form. For high Reynolds number flows, Reynolds-averaged Navier-Stokes simulations (RANS) are carried out using a turbulence model. The governing equations are as follows:

$$\frac{\partial \boldsymbol{Q}}{\partial t}+\frac{\partial\left(\boldsymbol{F}_j-\boldsymbol{F}_{V,j}\right)}{\partial x_j}=0, \tag{1}$$

where $\boldsymbol{Q}=[\rho,\rho u_i,\rho E]^T$ is the vector of conservative variables. $\boldsymbol{F}_j=\left[\rho u_j,\rho u_i u_j+p\delta_{ij},(\rho E+p)u_j\right]^T$ is inviscid flux, and $\boldsymbol{F}_{V,j} = \left[0, \tau_{ij}, \tau_{jk}u_k - q_j\right]$ denotes viscous flux ($i, j, k = 1,2$ for 2D, and $i, j, k = 1,2,3$ for 3D). Here, ρ is the density, u_i is the velocity, E is the total energy per unit mass, τ_{ij} is the viscous stress tensor, and q_j is the heat flux. The ideal gas law for relating the thermal quantities is

$$p = \rho RT, E = \frac{p}{\rho(\gamma - 1)} + \frac{1}{2}u_k u_k, \tag{2}$$

where T is the temperature, R is the gas constant, and γ=1.4 is the ratio of the specific heat. The viscous stress tensor and the heat flux are approximated as

$$\tau_{ij} = 2(\mu + \mu_t)\left[S_{ij} - \frac{1}{3}S_{kk}\delta_{ij}\right], \; q_j = -c_p\left(\frac{\mu}{Pr} + \frac{\mu_t}{Pr_t}\right)\frac{\partial T}{\partial x_j}, \tag{3}$$

where μ is the molecular viscosity, μ_t is the eddy viscosity for RANS, $S_{ij} = (\partial u_j/\partial x_i + \partial u_i/\partial x_j)/2$, and $c_p = \gamma R/(\gamma - 1)$ is the specific heat at constant pressure. Prandtl number Pr is set to 0.72, and turbulent Prandtl number Pr_t is set to 0.9. Spalart–Allmaras (SA) one-equation turbulence model [29] calculates the eddy viscosity. The version of SA used in this research is an SA-noft2 model [30], which neglects the f_{t2} term. The SA model is extended to a modified version of Delayed Detached-eddy simulation (DDES), which is called DDES-p [22,27]. It is well known that when the grid size in streamwise direction becomes small (comparable to the size of wall-normal direction), the switching point from large-eddy simulation (LES) to RANS model becomes closer to the wall. This leads to nonphysical flow separation. Therefore, DDES-p introduces a modified shielding function to protect the RANS regions when an isotropic cell that appears in the Cartesian grid is used. The original DDES length scale is described as

$$l_{DDES} \equiv (1 - f_d)l_{RANS} + f_d l_{DES}, \tag{4}$$

where l_{DDES}, l_{RANS}, and l_{DES} are the length scales for the original DDES, RANS(SA model) and DES, respectively. The function f_d is

$$f_d \equiv 1 - \tanh\left([8r_d]^3\right), \tag{5}$$

where

$$r_d \equiv \frac{\nu + \nu_t}{S\kappa^2 d^2}, \qquad S \equiv \sqrt{\frac{\partial u_i}{\partial x_j}\frac{\partial u_i}{\partial x_j}}. \tag{6}$$

The value $\kappa = 0.41$ is the von Karman constant, ν_t and ν are kinematic eddy viscosity and kinematic viscosity, respectively. To protect the LES regions, the length scale is modified as

$$l'_{DDES} \equiv (1 - \min(c_{d1}, f_d))l_{RANS} + \min(c_{d1}, f_d)l_{DES}, \tag{7}$$

where c_{d1} is a constant value of 0.5. By using the modified length scale, modified function f'_d is calculated as

$$f'_d \equiv 1 - \tanh\left([8r'_d]^3\right), \tag{8}$$

where

$$r'_d \equiv \frac{\nu + \nu_t\left(\frac{d}{l'_{DDES}}\right)}{S\kappa^2 d^2}. \tag{9}$$

The governing equations are discretized by the cell-centered finite volume method. The hierarchical Cartesian grid is treated as an unstructured grid data. The inviscid flux is evaluated using the Simple Low-dissipation advection upstream splitting method (SLAU) scheme [31]. The third-order monotonic upwind scheme for conservation laws (MUSCL) is used to increases spatial accuracy. The viscous flux is calculated using a modified second-order central difference [32]. The accuracy of the convective and diffusive flux of the SA model is second-order. We use the Green-Gauss method [33] to calculate the gradients of the primitive variables. Also, the LU-SGS method (an implicit time integration method) is used to calculate the time integration [34]. The summary of the numerical methods in the solver is listed in Table 1.

Table 1 – Summary of the numerical methods used in UTCart.

Governing equations	Compressible Navier-Stokes equations
Discretization Method	Cell-centered finite volume method
Turbulence model	DDES-p
Type of grids	Unstructured Cartesian grid with cell-based refinement
Inviscid flux	SLAU + 3rd order MUSCL scheme
Limiter	None
Viscous flux	2nd-order central difference
Gradient evaluation	Green-Gauss method
Time integration method	LU-SGS with dual time stepping, Constant dt
Wall boundary condition	Immersed boundary method (Wall function)

2.2 Immersed Boundary Method for UTCart

Figure 2 is the schematic of the grid near the wall boundary. The wall boundary condition is imposed at the center between the fluid cell and the wall cell (point face center (FC)). A discrete-forcing IBM is used to determine the boundary conditions. To determine the physical quantities of FC, an image point (IP) is set on the wall-normal line through FC, assuming one-dimensional variable profiles between the IP and the wall. The distance between the IP and the wall is $\mathrm{d_{IP}}$, related to the size of the ambient cells $\Delta\mathrm{x}$ by $\mathrm{d_{IP}} = \mathrm{r_{IP}}\Delta\mathrm{x}$. The constant value $\mathrm{r_{IP}}$ is the ratio of the IP distance to the cell size on the wall [35, 36]. The minimum value for $\mathrm{r_{IP}}$ is $\sqrt{2}$ in 2D and $\sqrt{3}$ in 3D for the IPs to be located in the fluid cells. The $\mathrm{r_{IP}}$ value is set to 3 in this study. The primitive variables $\mathbf{q}$ at the IP is linearly interpolated locally inside the cell and in combination with the wall boundary condition, the FC values are evaluated. In order calculate the turbulent boundary layer, SA based wall function proposed by Allmaras et al. [37] is used. Further details can be found in Tamaki et al. [24-26].

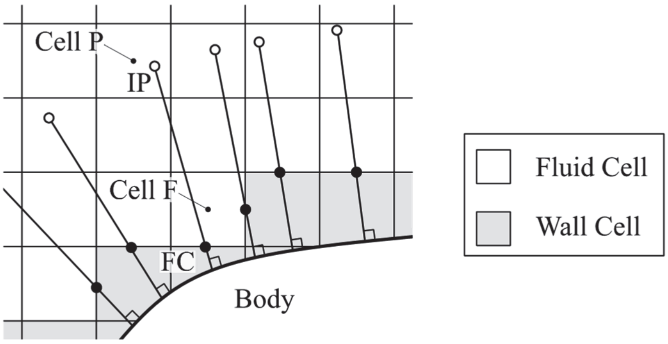

Figure 2 – Schematic of the wall boundary condition of the immersed surface.

2.3 Main Landing Gear Model of JAXA and the Flow Conditions

A non-sensitive two-wheel main landing gear digital model was designed by Japan Aerospace Exploration Agency (JAXA) to promote research for wind tunnel experiments as well as computational fluid dynamics (CFD) as shown in Fig. 3. This geometry is called “Landing gear noise Evaluation Geometry (LEG)”. The assumed aircraft is 100 PAX civil aircraft (two-engine wing mount), and the main landing gear is two-wheel landing gear which is typical for this size of aircraft. The digital model consists of large components (tires, cylinder, piston, doors, side-brace) and detail components (torque link, door operating rod, unlock actuator, uplock-pin, electrical wirings, and hydraulic tubes). Also, detailed geometries inside the tire, such as brake-caliper and wheel cap with cooling holes, are modeled. To avoid undesirable laminar flow separation on the tire surface, tripping tapes were applied when the wind tunnel experiment was performed. Therefore, it is also attached to the digital model on the upstream side of the tires. Reliable experimental results [5] are reported, therefore, it is a very good benchmark problem to assess the reliability of the numerical tools.

To investigate the contribution of each component to noise, flow simulations with component on/off is performed. The noise measurement study is often performed in the experiment in the same manner to understand the contribution of each component. Flow simulations are performed for seven different configurations that are summarized in Table 2. The Config. 1 is the simplest configuration that consists of only tires and a cylinder (only the grey components in Fig. 3). Meanwhile, the Config. 7 consists of all the components (full configuration) in Fig. 3. Other configurations are the model that consists of several landing gear components for better understanding the contribution from each component.

A typical approach speed of a civil transport aircraft is assumed to be 68.0m/s, but it is well known that the local flow field around the landing gear is reduced due to the presence of extended high-lift-devices [2,4]. Therefore, the mean flow velocity is assumed to be 80% of the approach speed; 54.4m/s. The angle-of-attack and side-slip-angle are set to 0 degrees. The Reynolds number based on the diameter of the tire D (0.417m for 40% scale wind tunnel model) and the freestream velocity is 1.55×10^6.

In our previous study [22], flow simulation around the LEG model was performed using three different grid resolutions, and the finest grid resolution is chosen throughout this study (See Fig.4). The outer boundary of the computational domain is rectangular (200D×40D×40D). The minimum grid size dxmin near the landing gear surface is kept constant (0.0024D = 1.0mm). The refinement box region ($-1 \le x/D \le 4$, $-2 \le y/D \le 2$, $0 \le z/D \le 3$) is applied around the landing gear so that the eddies in the wake and acoustic wave can be captured within this region. The grid size in the refinement box region is chosen to be 0.010D (4 times of the minimum grid size). If we assume 20 points per wave is necessary to resolve the propagation of acoustic wave, and ignore the Doppler effect, acoustic wave frequency up to 4 kHz can be resolved in the simulation.

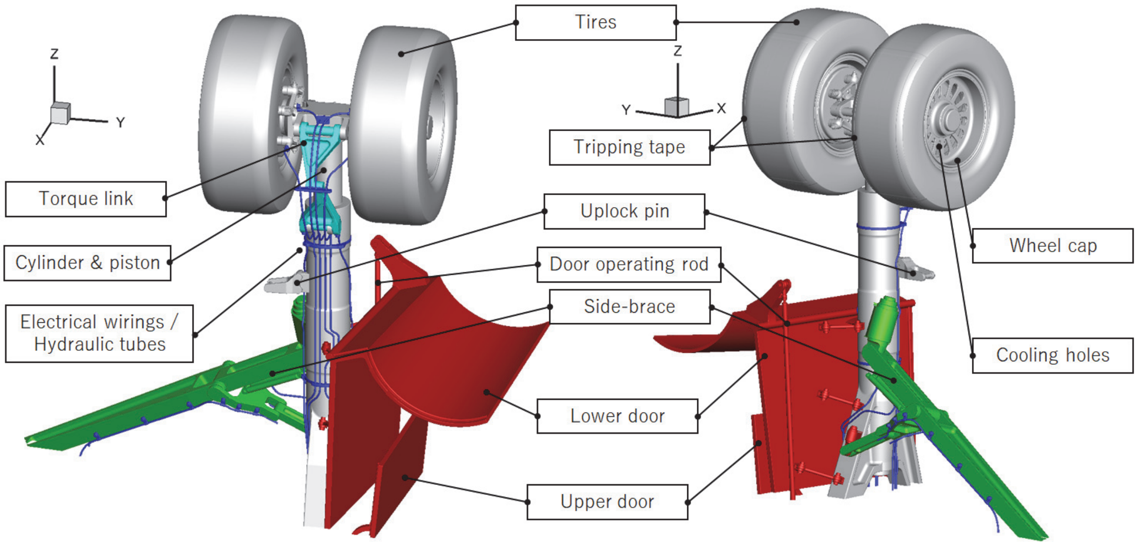

Figure 3 – JAXA LEG model (Fully dressed without cavity).

The total grid points of the seven configurations varies from 75 to 82 million as summarized in Table 2. The grid generation time on a single core (Intel® Xeon® CPU E5-2620 v4 @ 2.10GHz) is approximately 2hours. Note that the grid generation is performed automatically once after the input parameters for the grid generation is fixed. A symmetric boundary condition is applied on the wall where the landing gear is attached, and subsonic far-field boundary conditions which is determined based on the method proposed by Chakravarthy [38] is applied to the rest of the five planes.

The initial flow field is generated based on RANS (SA using wall function for IBM [24-26]) assuming steady-state flow. Then, unsteady flow simulation is performed switching to DDES-p mode. The numerical simulations were run over a duration that consist of more than 60 tire diameter flow-through time units, which consists of about T=0.490s. The statistical data shown in this study is generated from the latter half of the unsteady flow simulations (T=0.245s). A dual time stepping method is used for the unsteady flow simulation. The LU-SGS implicit scheme is used for the inner iteration to remove the restriction of Courant-Friedrichs-Lewy condition. The number of inner iterations is fixed to 4. The time increment dt is 0.01. The time increment for each case is selected so that the Courant number based on the sonic speed c_∞ will be approximately 1 in the refinement box region. If we assume 20 points is necessary temporary to resolve the acoustic wave, the upper limit of the resolvable frequency is estimated to be around 4kHz.

The flow simulations are performed using a supercomputer system (Oakbridge-CX) operated by the Information Technology Center, The University of Tokyo. All the simulations were performed using 784 cores and the computational time for obtaining the statistical data was approximately 11 hours. The overall simulation time starting from grid generation were performed within a day per one configuration.

Table 2 – Summary of landing gear configurations.

Config.	Tire & Cylinder	Doors	Side-brace	Torque-link	Wiring & Tubes	Number of cells
1	✓					74,836,875
2	✓	✓				79,962,037
3	✓		✓			76,458,671
4	✓			✓		75,091,948
5	✓			✓	✓	75,966,282
6	✓	✓	✓	✓		81,816,967
7	✓	✓	✓	✓	✓	82,416,988

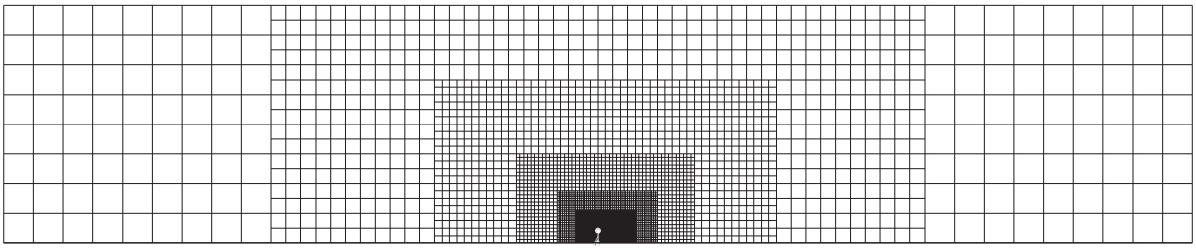

(a) Overall view

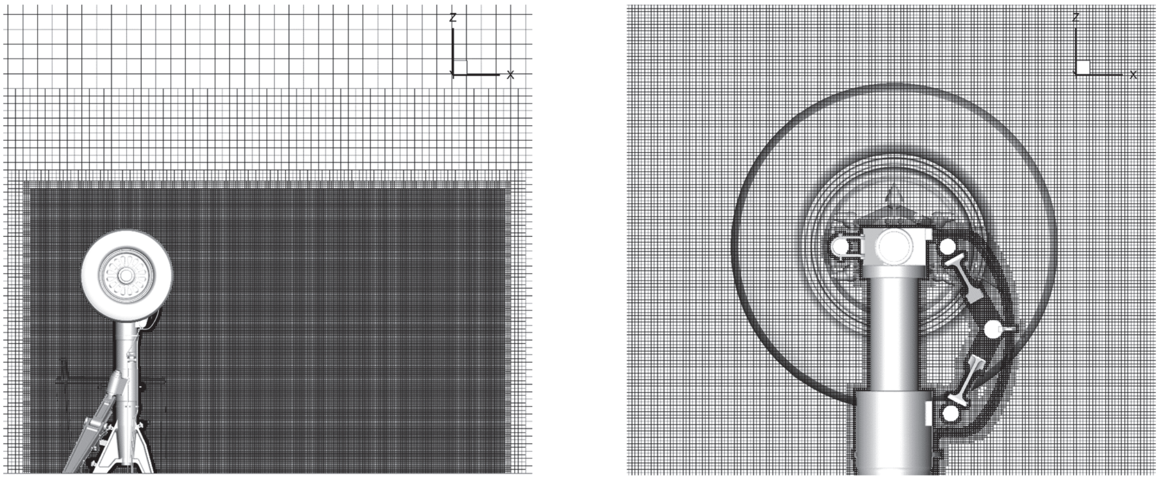

(b) Grid near the LEG model with refined region

(c) Grid between the tire

Figure 4 – Computational grid around the LEG model on *xz*-plane (*y*=0, Config. 7).

3. Computational Results

3.1 Analysis around the full configuration (Config. 7)

Figure 5 describes the time-averaged pressure coefficient (Cp) distribution on the surface of Config. 7. On the front side of the model (See Fig. 5 (a)), stagnation pressure (Cp=1) is observed on all the components. Meanwhile, low-pressure area is observed on the rear side of the model (See Fig. 5 (b)). Most area is inside the separated flow, and regions lower than Cp=-1 are observed locally around the tire and the doors. The low-pressure area on the upper door is due to the longitudinal vortex originated from the door opening rod. The time-averaged Cp along the centerline of both tires (door and side-brace sides) are compared with that of the experimental results [5] in Fig. 6. The lines are the numerical results, and the symbols are the experimental results. The overall trend of Cp shows good agreement on the two tires. The spikes observed in the numerical results (around θ=120 and 230 degrees) are due to the tripping tapes. Additionally, the Cp difference is observed between θ =90 to 180 degrees in the experiment. The Cp values are slightly lower on the door side compared to those on the Side-brace side. This tendency is also observed in our numerical results.

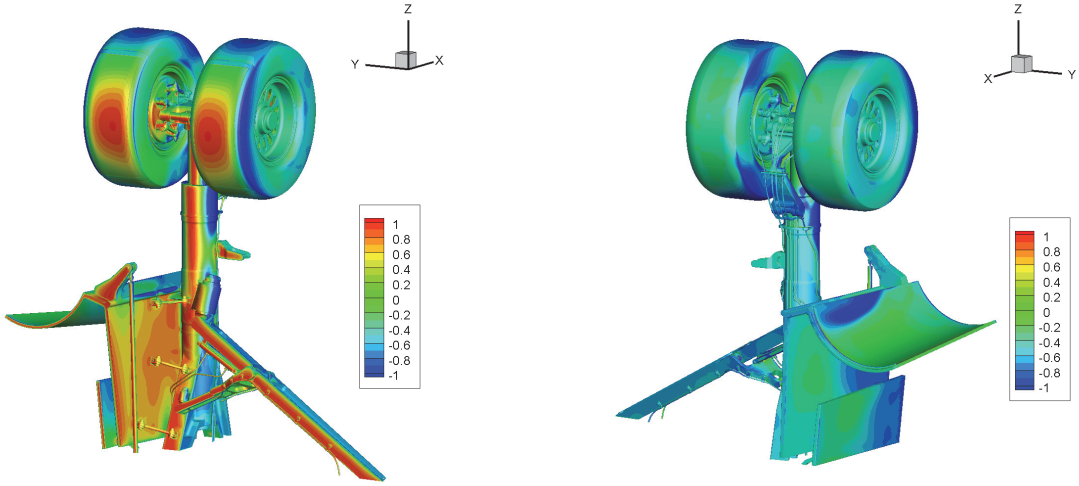

(a) Front view (b) Rear view

Figure 5 – Surface Cp distributions (Config. 7).

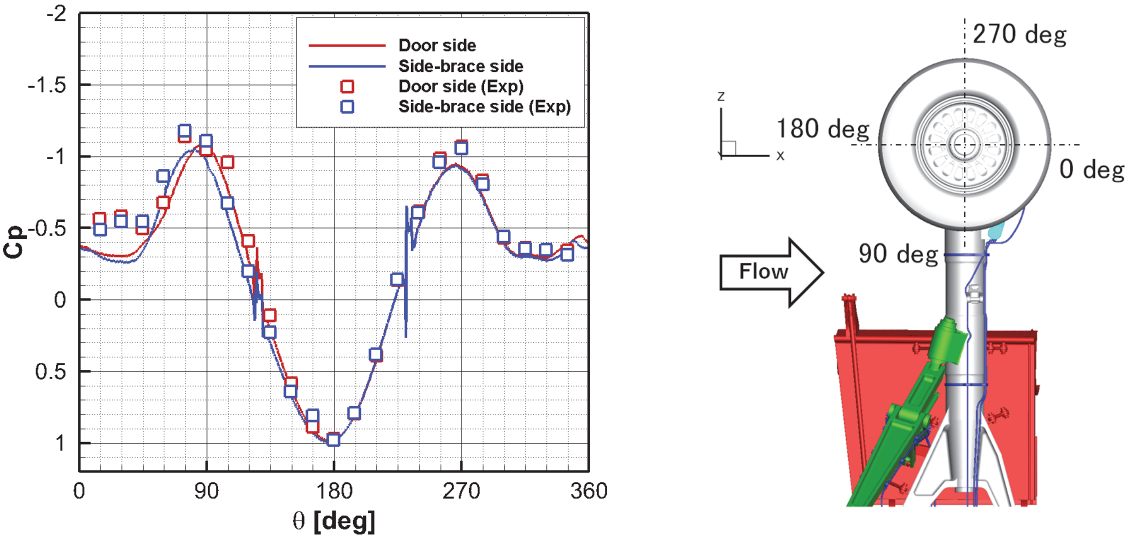

Figure 6 – Comparison of surface Cp distributions between the result (Config. 7) and the experimental data [5].

The time-averaged velocity field around the model on three different cross-sections is described in Fig. 7. The plane, y=0, is located in between the tires. A strong shear layer from the tip of the piston is observed. The plane z=2D is slightly lower than that of the tire axel and crosses the cooling holes of the wheel caps. A shear layers from the shoulder of the tires are observed and an accelerated region between the tires and the piston is present. Also, the flow through the cooling holes is observed. The plane x=0.11D is located slightly downstream side of the tire axel. Accelerated flow around the tire and the wake region behind the components are observed.

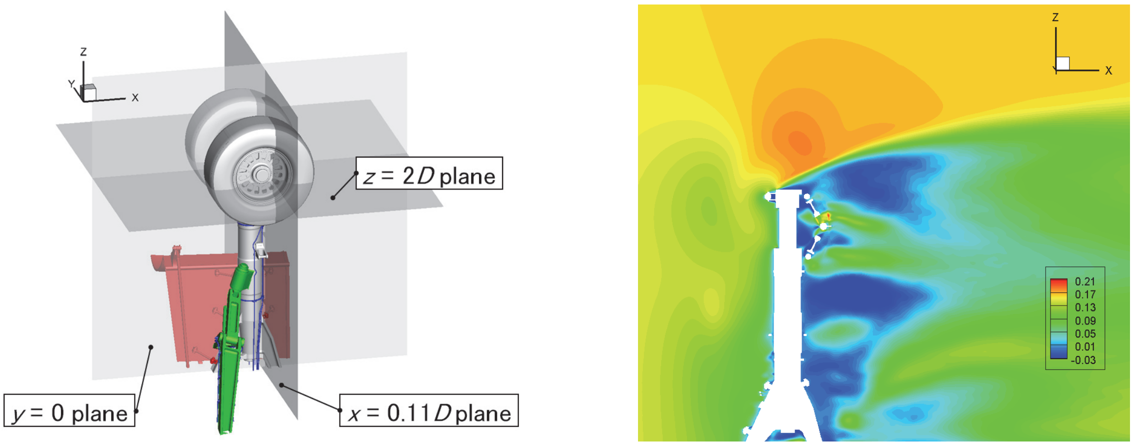

(a) *y*=0 cross section

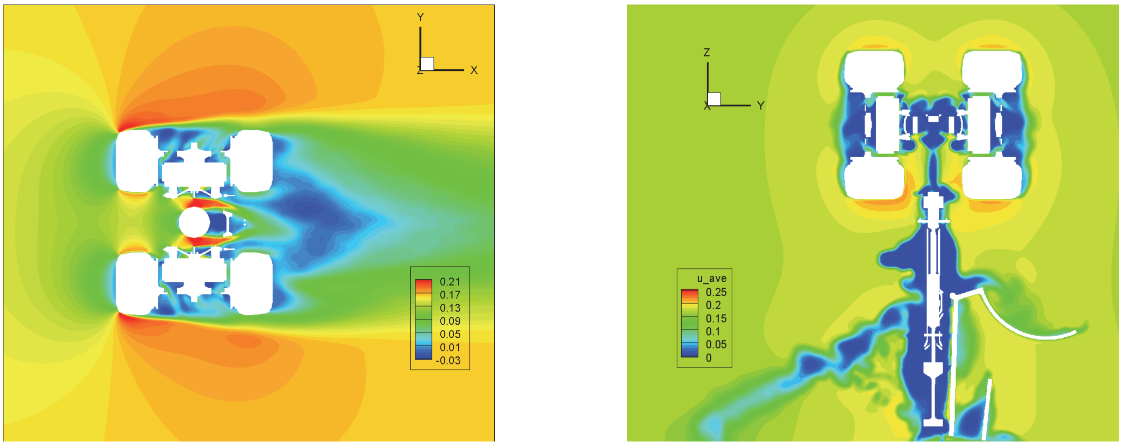

(b) *z*=2*D* cross section

(c) *x*=0.11*D* cross section

Figure 7 –Time-averaged streamwise velocity (u_{ave}) contour (Config. 7).

The root-mean-square of the pressure coefficient ($C_{p,rms}$) on the model surface is visualized in Fig. 8. Comparing the views from the front and rear sides, the $C_{p,rms}$ on the rear side is relatively larger. Especially, large fluctuation is observed around the sidewall of the tires and the wheel cap. The fluctuation is also large around the downstream of the door operating rod.

By assuming that acoustic sources are compact, the acoustic pressure is evaluated using Curle's equation. The pressure p_a at point $\boldsymbol{x}$ is estimated as follows.

$$p_a(\boldsymbol{x}) = \frac{1}{4\pi c}\frac{x_i}{|\boldsymbol{x}|^2}\frac{\partial}{\partial t}\int_S n_i p dS\,. \tag{10}$$

The value c is the sonic speed, S is the body surface, n_i is the unit normal vector on the body surface, and p is the pressure on the body. The integral in the equation describes the aerodynamic force vector on the LEG model, thus the acoustic pressure can be evaluated through a simple numerical procedure.

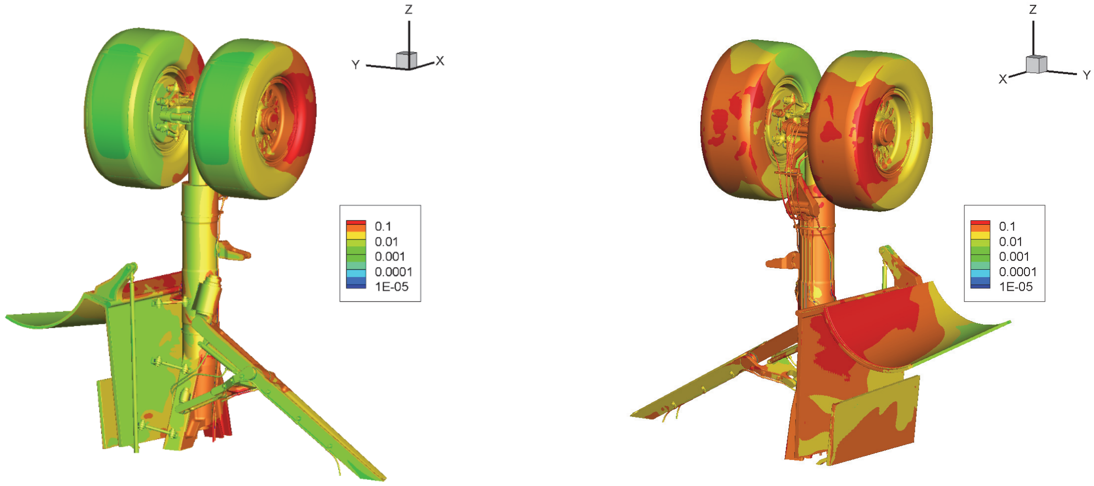

(a) Front view (b) Rear view

Figure 8 –Surface $C_{p,rms}$ distributions (Config. 7).

The unsteady pressure at a distance of 5m (12.0*D*) assuming a compact noise source at the center of the tire axel (0.0, 0.0, 2.1*D*) are evaluated for Config. 7, and the power spectrum density (PSD) is shown in Fig. 9. The acoustic signal based on the integration of each component are also calculated to investigate the contribution. Note that surface pressure fluctuation on one component might be affected by the other components, therefore the indirect contribution of the other components is also included. The dominant noise components around 1kHz are the Doors followed by Tire&Cylinder and Torque-link. Meanwhile, the simulation is based on a 40% scale wind tunnel model. Therefore, fluctuation at 2.5kHz in this simulation corresponds to 1kHz of the full-scale model. The dominant noise components around 2.5kHz are Tire&Cylinder followed by Doors and Torque-link. The contribution of Side-brace is apparent at low frequency (200 to 500Hz) but not over 1kHz. The contribution of the Torque-link to the acoustic signal is larger than the Side-brace at 2.5kHz. The effect of the Wiring&tubes is negligible compared to the dominant components.

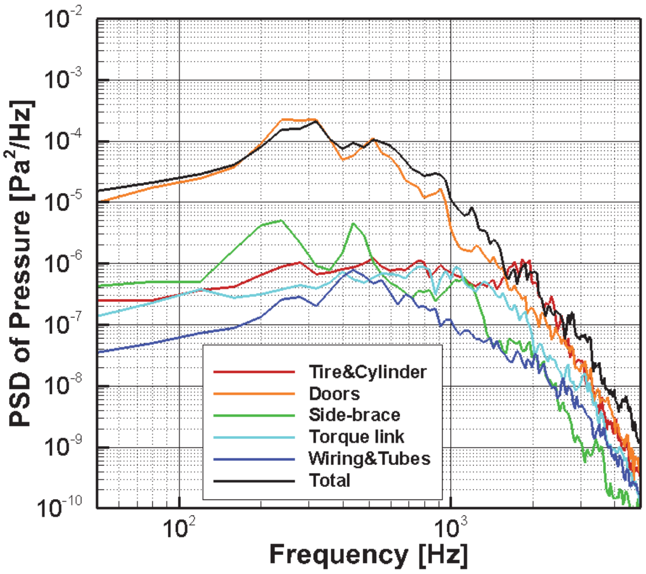

Figure 9 –PSD of pressure of Config.7 and its component-wise contribution.

3.2 Investigation of components on/off effect

Figure 10 describes the time-averaged pressure coefficient (Cp) distribution on the surface of

Config. 1 to 6. The figures in the box are the partial view between the tires from the rear side. The Cp distributions around the landing gear show similar patterns among different configurations. Additionally, the Cp distribution pattern on each component is similar to that of Config. 7 shown in Fig. 5.

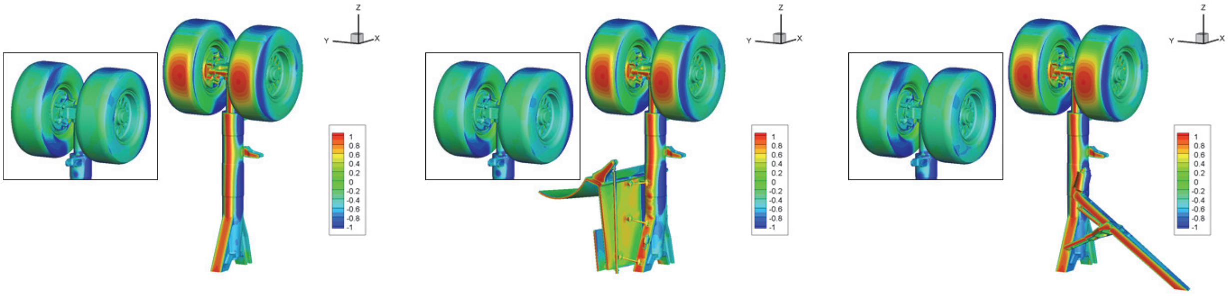

a) Config. 1 b) Config. 2 c) Config. 3

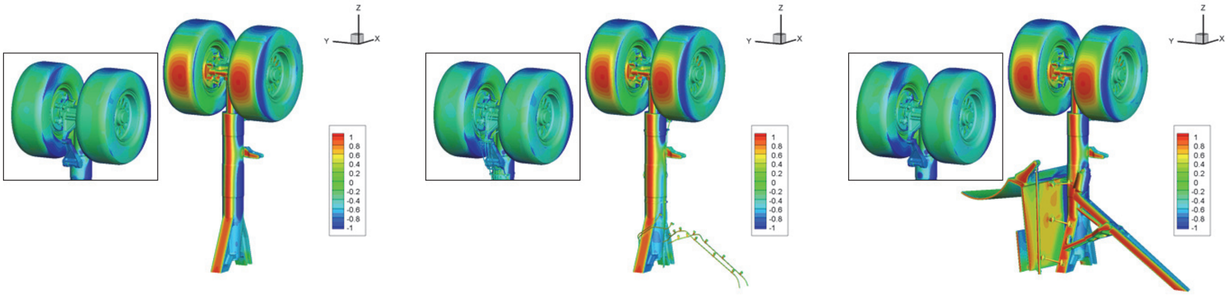

d) Config. 4 e) Config. 5 f) Config. 6

Figure 10 – Surface Cp distributions (Config. 1 to 6).

The overall sound pressure level (OASPL) at a distance of 5m (12.0*D*) assuming a compact noise source at the center of the tire axel (0.0, 0.0, 2.1*D*) are evaluated on seven different configurations, and Table 3 lists the results. The largest OASPL is observed for Config. 7 followed by Configs. 6 and 2. The configurations which include the Doors have large OASPL values, thus, the Doors are the dominant component. Additionally, the OASPL of each component is summarized in Table 3. It is noteworthy that the standard deviation (SD) of OASPL for each component is relatively low (less than 2dB) for most components. For example, OASPL values of Torque-link vary within the range of 60.4 to 63.8dB (SD is 1.6dB) among different configurations (Config. 4 to 7). One exception is the OASPL of Tire&Cylinder. The OASPL of Config. 1 to 6 varies within the range of 71.4 to 73.8dB, but that of Config. 7 is 65.9dB, which is approximately 6dB lower than the other configurations. Especially, the difference in geometry between Configs. 6 and 7 is only the Wiring&Tubes. To better understand this phenomenon, the PSD of Tire&Cylinder for Config. 1 to 7 is drawn in Fig. 11. The PSD distribution of Config. 7 is different from the others, especially below 1kHz. Also, a small peak is observed around 2kHz for Config. 7. For Config. 1 to 6, the PSD level below 1kHz is similar, but the discrepancy is observed over 1kHz. We must keep in mind that even if the OASPL difference is small, there may be a difference in the PSD distribution. It is still an open question whether we can achieve a grid convergence on the flow simulation around complex geometry such as realistic landing gear. In our previous study [5], we have performed a grid convergence study and observed the tendency of the grid convergence, but complete grid convergence was unachieved. Therefore, the results may change if we further refine the grid. However, the current results show that the OASPL (or PSD) differs even with the same component among different configurations.

Finally, a comparison of PSD of pressure between different configurations is shown in Fig 12. Once again, the PSD levels are high for Configs. 2, 6, and 7 which include Doors. The dominant noise components around 1kHz are the Doors followed by Side-brace and Torque-link. Meanwhile, the dominant noise components around 2.5kHz are Doors followed by Torque-link and Side-brace. In Fig. 9, Tire&Cylinder appears as one of the main noise sources, but this is unclear for both frequencies in Fig. 12. The evidence suggests that simple comparison by putting on/off the components may not be appropriate when we need to understand the contribution of the components to the far-field noise in detail.

Table 3 – OASPL of 7 configurations and contribution of components.

Config.	Tire & Cylinder	Doors	Side-brace	Torque-link	Wiring & Tubes	Total
1	71.4 dB					71.4 dB
2	73.8 dB	80.6 dB				81.5 dB
3	73.1 dB		66.7 dB			74.0 dB
4	72.6 dB			60.5 dB		72.9 dB
5	72.3 dB			60.4 dB	55.7 dB	73.2 dB
6	73.2 dB	81.2 dB	67.8 dB	63.8 dB		82.0 dB
7	65.9 dB	81.8 dB	65.2 dB	63.4 dB	59.0 dB	82.3 dB
SD	2.5 dB	0.5 dB	1.1 dB	1.6 dB	1.6 dB	

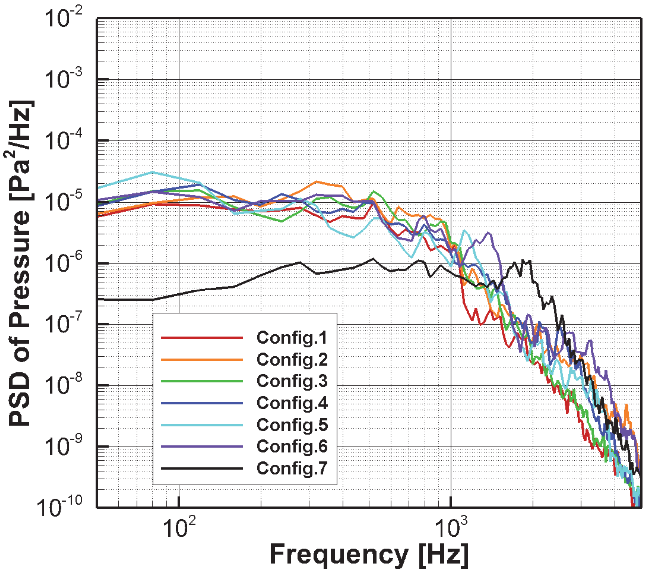

Figure 11 –PSD of pressure from Tire&Cylinder for 7 configurations.

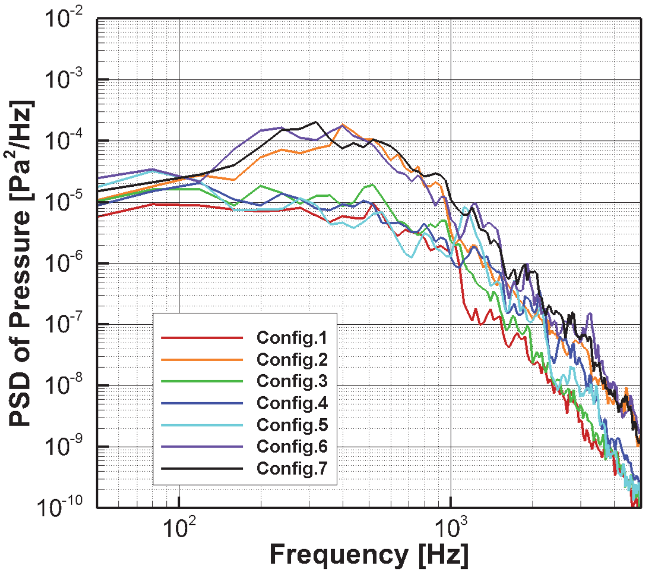

Figure 12 –PSD of pressure for 7 configurations.

4. Conclusions

The noise generated from a realistic landing gear configuration was investigated through flow simulations around multiple configurations by putting on/off the landing gear components. The simulations were performed by using the Navier-Stokes equation-based flow solver on the non-body-fitted Cartesian grid. Near wall boundary condition was imposed using an immersed boundary method, and DDES based turbulence model modified for the applications on the non-body-fitted Cartesian grid was used to simulate the unsteady flow. The overall flow field around the complex geometry was investigated in detail based on the time-averaged flow field. The Cp distribution around both tires showed reasonable agreement with the experimental data. Also, the far-field noise is estimated based on Curle's equation assuming that acoustic sources are compact. We have investigated the relationship between the landing gear components and the power spectral density distribution. The dominant component below 1kHz was Doors, and that at 2.5kHz (corresponds to 1kHz in the full-scale model) was Tire&Cylinder followed by Doors and Torque-link. From components on/off simulations, the OASPL (or PSD) differs even with the same element among different configurations. Also, the order of contribution to the far-field noise does not always match with that of full configuration (Config. 7). The evidence suggests that simple comparison by putting on/off the components may not be appropriate when we need to understand the contribution of the components to the far-field noise in detail.

5. Acknowledgement

The LEG geometry was kindly provided by Aeronautical Technology Directorate of Japan Aerospace Exploration Agency. Author would like to express his gratitude for their contribution. This research was conducted using the Fujitsu PRIMERGY CX2550M5/CX2560M5(Oakbridge-CX) in the Information Technology Center, The University of Tokyo.

6. Copyright Statement

The authors confirm that they, and/or their company or organization, hold copyright on all of the original material included in this paper. The authors also confirm that they have obtained permission, from the copyright holder of any third party material included in this paper, to publish it as part of their paper. The authors confirm that they give permission, or have obtained permission from the copyright holder of this paper, for the publication and distribution of this paper as part of the ICAS proceedings or as individual off-prints from the proceedings.

References

[1] Lockard, D., Khorrami, M., & Li, F. Aeroacoustic analysis of a simplified landing gear. *9th AIAA/CEAS Aeroacoustics Conference and Exhibit*. 2003-3111. (2003).

[2] Guo, Y. A study on local flow variations for landing gear noise research. *14th AIAA/CEAS Aeroacoustics Conference (29th AIAA Aeroacoustics Conference).* 2008-2915. (2008).

[3] Keating, A., Dethioux, P., Satti, R., Noelting, S., Louis, J., Van de Ven, T., & Vieito, R. Computational aeroacoustics validation and analysis of a nose landing gear. *15th AIAA/CEAS aeroacoustics conference (30th AIAA aeroacoustics conference).* 2009-3154. (2009).

[4] Imamura, T., Hirai, T., Amemiya, K., Yokokawa, Y., Enomoto, S., & Yamamoto, K. Aerodynamic and aeroacoustic simulations of a two-wheel landing gear. *Procedia Engineering*, 6, 293-302. (2010).

[5] Yokokawa, Y., Imamura, T., Ura, H., Uchida, H., Yamamoto, K., & Kobayashi, H. Experimental study on noise generation of a two-wheel main landing gear. *16th AIAA/CEAS Aeroacoustics Conference.* 2010-3973. (2010).

[6] Onda, H., Sakai, R., Sasaki, D., & Nakahashi, K. Unsteady flow and aerodynamic noise analysis around JAXA landing gear model by building-cube method. *49th AIAA Aerospace Sciences Meeting including the New Horizons Forum and Aerospace Exposition.* 2011-1081. (2011).

[7] Murayama, M., Yokokawa, Y., Kato, H., Ura, H., Uchida, H., Yamamoto, K., Abe, K., & Wu, L. Computational and experimental study on noise generation from tire-axle regions of a two-wheel main landing gear. *17th AIAA/CEAS Aeroacoustics Conference (32nd AIAA Aeroacoustics Conference).* 2011-2821. (2011).

[8] Vatsa, V., Lockard, D., & Khorrami, M. Application of FUN3D solver for aeroacoustic simulation of a nose landing gear configuration. *17th AIAA/CEAS Aeroacoustics Conference (32nd AIAA Aeroacoustics Conference).* 2011-2820. (2011).

[9] Ueno, Y., Nagata, T., Ochi, A., & Hayama, K. Aeroacoustic analysis of the rudimentary landing gear using octree unstructured grid with boundary-fitted layer. *18th AIAA/CEAS Aeroacoustics Conference (33rd AIAA Aeroacoustics Conference).* 2012-2284. (2012).

[10] Murayama, M., Yokokawa, Y., & Yamamoto, K. Computational study on noise generation from a two-wheel main landing gear. *28th International Congress of the Aeronautical Sciences* (pp. 1-14). (2012).

[11] Murayama, M., Yokokawa, Y., Yamamoto, K., & Hirai, T. Computational study of low-noise fairings around tire-axle region of a two-wheel main landing gear. *Computers & Fluids*, 85, 114-124. (2013).

[12] Langtry, R. B., Larssen, J. V., Winkler, C. M., Dorgan, A. J., & Mani, M. DDES and acoustic prediction of rudimentary landing gear experiment using unstructured finite volume methods. *Flow, turbulence and combustion*, 91(3), 717-745. (2013).

[13] Casalino, D., Ribeiro, A. F., Fares, E., & Nölting, S. Lattice–Boltzmann aeroacoustic analysis of the LAGOON landing-gear configuration. *AIAA journal*, 52(6), 1232-1248. (2014).

[14] Brionnaud, R., Chávez Modena, M., Trapani, G., & M. Holman, D. Direct Noise Computation with a Lattice-Boltzmann Method and Application to Industrial Test Cases. *22nd AIAA/CEAS Aeroacoustics Conference*. 2016-2969. (2016).

[15] Murayama, M., Takaishi, T., Ito, Y., Yokokawa, Y., Yamamoto, K., Sakai, R., Hirai, T., & Tanaka, K. Numerical Simulation of Main Landing Gear Noise Reduction in FQUROH Flight Demonstration. *AIAA Scitech 2019 Forum.* 2019-1836. (2019).

[16] Duda, B. M., Ferris, R., & Khorrami, M. R. Simulation-Based Assessment of a Full-Scale Installed Quiet Landing Gear. *25th AIAA/CEAS Aeroacoustics Conference.* 2019-2476. (2019).

[17] Ito, Y., Yokokawa, Y., Takaishi, T., Yamamoto, K., Hirai, T., Ueno, Y., Isotani, K., Hayama, K., Shimada, A., Kumada, T., & Hayashi, K. Noise Reduction of Regional Jet Two-Wheel Main Landing Gear. *25th AIAA/CEAS Aeroacoustics Conference.* 2019-2481. (2019).

[18] Vuillot, F., Landier, S., Renaud, T., Benoît, C., & Sanders, L. Intersected Octree Conformal Grid Strategies for Applications to Aeroacoustic Computations of the LAGOON, Landing Gear Model, Using the CEDRE Unstructured Flow Solver. *25th AIAA/CEAS Aeroacoustics Conference.* 2019-2483. (2019).

[19] Ueno, Y., Isotani, K., Hayama, K., Takaishi, T., Ito, Y., Yokokawa, Y., Murayama, M., & Yamamoto, K. Validation of Noise Reduction Design for Landing Gear in the FQUROH Flight Demonstration Project. *25th AIAA/CEAS Aeroacoustics Conference.* 2019-2506. (2019).

[20] Ueno, Y., & Ochi, A. Airframe Noise Prediction Using Navier-Stokes Code with Cartesian and Boundary-fitted Layer Meshes. *25th AIAA/CEAS Aeroacoustics Conference.* 2019-2553. (2019).

[21] Kiris, C., Barad, M., & Kocheemoolayil, J. LAVA Lattice Boltzmann Development/Application to Landing Gear. (2019).

[22] Imamura, T, and Tamaki, Y. Unsteady Flow Simulation around Two-Wheel Main Landing Gear based on Compressible Navier-Stokes Solver with Immersed Boundary Method. AIAA AVIATION 2020 FORUM. 2020-2579. (2020).

[23] Imamura, T., Tamaki, Y., & Harada. M., Parallelization of a compressible flow solver (UTCart) on cell-based refinement Cartesian grid with immersed boundary method, *Proceedings of the 29th International Conference on Parallel Computational Fluid Dynamics.* (2017).

[24] Tamaki, Y., Harada, M., & Imamura, T. Near-wall modification of Spalart–Allmaras turbulence model for immersed boundary method. *AIAA Journal*, 3027-3039. (2017).

[25] Tamaki. Y., Turbulent Flow Simulations around Aircraft using Hierarchical Cartesian Grids and the Immersed Boundary Method, *Ph.D Dissertation Thesis of the University of Tokyo*, March 2018.

[26] Tamaki, Y., & Imamura, T. Turbulent flow simulations of the common research model using immersed boundary method. *AIAA Journal*, 56(6), 2271-2282. (2018).

[27] Tamaki, Y., & Imamura, Effect of the Boundary-Layer Shielding Function on Delayed Detached-Eddy Simulation of Transonic Buffet. *Annual Meeting of the Japan Society of Aeronautical and Space Sciences.* 49, (2018). (in Japanese)

[28]METIS - serial graph partitioning and fill-reducing matrix ordering, http://glaros.dtc.umn.edu/gkhome/metis/metis/overview, retrieved on May 29, 2021.

[29] Spalart, P., & Allmaras, S. A one-equation turbulence model for aerodynamic flows. *30th aerospace sciences meeting and exhibit.* 92-0439. (1992).

[30] NASA, Turbulence Modeling Resource, http://turbmodels.larc.nasa.gov/, retrieved on May 29, 2021.

[31] Shima, E., & Kitamura, K. Parameter-free simple low-dissipation AUSM-family scheme for all speeds. *AIAA journal*, 49(8), 1693-1709. (2011).

[32] Wang, G., Schwöppe, A., & Heinrich, R. Comparison and Evaluation of cell-centered and cell-vertex discretization in the unstructured Tau-code for turbulent viscous flows. *ECCOMAS CFD* (Vol. 2010). (2010, June).

[33] Shima, E., et al., Green-Gauss/Weighted-Least-Squares Hybrid Gradient Reconstruction for Arbitrary Polyhedra Unstructured Grids, AIAA Journal 51(11) 2740-2747. (2013)

[34]Yoon, S., & Jameson, A. Lower-upper symmetric-Gauss-Seidel method for the Euler and Navier-Stokes equations. *AIAA journal*, 26(9), 1025-1026. (1988).

[35] Capizzano, F. Turbulent wall model for immersed boundary methods. *AIAA journal*, 49(11), 2367-2381. (2011).

[36] Berger, M. J., & Aftosmis, M. J. An ODE-based wall model for turbulent flow simulations. *AIAA Journal*, 700-714. (2018).

[37] Allmaras, S. R., & Johnson, F. T. Modifications and clarifications for the implementation of the Spalart-Allmaras turbulence model. *Seventh international conference on computational fluid dynamics (ICCFD7)* (pp. 1-11). (2012).

[38] Chakravarthy, S. R., & Osher, S. Numerical experiments with the Osher upwind scheme for the Euler equations. *AIAA journal*, 21(9), 1241-1248. (1983).